https://doi.org/10.1016/j.addma.2024.104125

The enhancement of damage tolerance of 3D-printed high strength architected metallic glasses by unit cell shape design

Congrui Yang[1, 2], Di Ouyang[1,3], Lei Zhang[3], Yongyun Zhang[1, 2], Xing Tong[2], Haibo Ke[2*], K.C. Chan[1*], Weihua Wang[2,4]

1. Research Institute for Advanced Manufacturing, Department of Industrial and Systems Engineering, The Hong Kong Polytechnic University, Hong Kong, China.

2. Songshan Lake Materials Laboratory, Dongguan, 523808, China

3. State Key Laboratory of Material Processing and Die & Mould Technology and School of Materials Science and Engineering, Huazhong University of Science and Technology, Wuhan, 430074, China

4. Institute of Physics, Chinese Academy of Sciences, Beijing 100190, China

[*] Corresponding author.
E-mail address: kc.chan@polyu.hk (Kang Cheung Chan), kehaibo@sslab.org.cn (Haibo Ke)

Abstract

In this work, we developed a strategy that can simultaneously enhance the strength and energy absorption of 3D-printed architectural Zr-based bulk metallic glass (BMG) through unit cell shape design. Strut-based body-centered tetragonal (BCT) with different scaling degrees were incorporated into the conventional metallic glass architectures to avoid the fast propagation of main crack bands and induce multiple micro fracturing of the metallic glass (MG) lattices. Thus, the failure characteristics of 3D-printed architectural BMG underwent a remarkable transformation from a catastrophic fracture to a sequential localized fracture, which effectively overcomes catastrophic failure. It is evidenced by the emergence of a smooth plateau in the stress-strain curves, signifying enhanced damage tolerance. Consequently, the energy absorption capacity increased by 2.2 times, with the compressive strength increased by various degrees compared to the body centered cubic (BCC) structure, indicating the viability of this shape design strategy. Therefore, this work provides a novel route for material-structure-combined design to simultaneously improve the strength and energy absorption of BMG. This breakthrough also enables architected MGs to overcome their inherent extreme brittleness, unlocking their vast potential for crafting impact-resistant and energy-absorbing intricate structural components through lightweight design.

Keywords: Bulk metallic glasses; Additive manufacturing; Lattice structures; Damage tolerance

1. Introduction

In future deep space exploration, spacecrafts will encounter increasingly complex and variable environments. Their internal precision instruments will impose higher demands on load-bearing and protective structures. It has already been observed that small size of debris can potentially cause damage to operational space systems. Spacecraft architects incorporate implicit protection into the vehicle architecture to mitigate the risk of function loss or mission failure resulting from collisions with small sized debris, especially particles ranging from 1 to 5 mm in diameter [1]. Hence, Structural materials must meet specific criteria for the mechanical properties of advanced aerospace materials, including high strength, impact resistance, and excellent energy absorption capabilities.

Though the above crystallized metallic structural materials boast impressive mechanical properties, they fall short of meeting the rigorous requirements of future aerospace materials. Bulk metallic glasses (BMGs) hold a prominent position in the realm of spacecraft materials due to their advantages such as high hardness, high strength, large elastic limits etc. [2], and have become a highly coveted materials in both spacecraft shielding and advanced structural applications [3-8]. In addition to its excellent mechanical properties, BMGs exhibit distinctive functional characteristics [9-13], including biocompatibility [14], catalytic properties [15], corrosion resistance [14], wear resistance [16], optical properties, soft magnetic properties and energy absorption capacity.

However, research on BMGs structural materials has remained stagnant due to the challenges posed by the large-scale production and their inherent brittleness at room temperature. Particularly, research regarding 3D-printed structural BMGs as energy-absorbing materials is rarely reported. In this case, the relationship between the lattice structure and damage tolerance, as well as other mechanical properties, remains unclear. The exploration of energy absorption in BMG structures is still largely confined to the 2D or microscopic level [17, 18].

Conventional fabrication methods are incapable of producing BMGs with complex shapes

due to the requirement of having a sufficiently high cooling rate. In recent years, the emergence of additive manufacturing (AM) technology, with its layer-by-layer processing capabilities, has enabled the production of fully glassy components with intricate shapes [19, 20]. This development offers a new approach to address the two challenges associated with amorphous alloy forming: size limitations and shape constraints [15, 21]. The compressive strength of 3D-printed BMGs (1000-2500 MPa) is comparable to that of as-cast BMGs [19]. By utilizing AM technology, structural BMGs can be designed and fabricated with tailored mechanical properties to meet the specific demands of the aerospace applications. Compared to random foams, lattice structures composed of periodic repeating unit cells offer a higher degree of designability and controllability [22], making them more suitable for comprehensively summarizing deformation behavior and pursuing higher performance.

The body centered cubic (BCC) structure is the most common and well studied strut-based structure [23]. With its simple configuration, it is suitable for establishing the structure-property relationship for new materials. Besides, triply periodic minimal surface (TPMS) structures, a novel lattice structure, are intriguing for their uninterrupted and sleek surfaces, facilitating extensive surface areas and unbroken internal passages. The diamond lattice (D-TPMS) is a type of TPMS structure that exhibits superior energy absorption capabilities compared to other TPMS structures [24]. TPMS lattice structures offer potential advantages over strut-based lattices in terms of manufacturability and mechanical properties, as they exhibit zero mean curvature at every point, thereby avoiding stress concentration at the nodes.

In this paper, utilizing the AM technology, we fabricated the 3D lattices BMG with a strut-based BCC lattice and a sheet-based TPMS lattice. Subsequently, an investigation of the compressive deformation behavior of the 3D-printed architectural BMG was conducted to establish a structure-property relationship for guiding future BMG structural designs. It was found that the issue of extreme brittleness remains a significant challenge in the context of BMG lattice structures. The D-TPMS lattices failed to demonstrate their superior energy absorption capabilities due to catastrophic failure. In contrast, BCC lattices exhibited better adaptability to the brittle BMG due to continuous crushing. Drawing inspiration from unit cell

designs with the potential to alter deformation behavior, we formulated a novel structural design strategy that optimizes unit cell configurations within BCC lattices [25]. The body-centered tetragonal (BCT) unit cell can be envisioned as a variation of the body-centered cubic (BCC) unit cell, with a slight decrease in height along one direction, where $a = b \neq c$. As the BCC unit cell transforms into the BCT unit cell, alterations in stress distribution within the lattices result in the initiation of microfractures in struts. This leads to the progressive formation and propagation of crack bands, thereby avoiding catastrophic failure. Subsequently, the proposed design strategy was evaluated in the framework of the BCC structure with different strut lengths, and finally achieved the simultaneous enhancement of compressive strength and energy absorption capacity. More importantly, our strategy effectively changed the failure mode of the structural BMGs, marking a significant step toward addressing the challenge of brittleness in BMG lattice structures.

2. Materials and methods

2.1 Manufacture and modeling of lattice structures

Gas-atomized equimolar $Zr_{60.14}Cu_{22.31}Fe_{4.85}Al_{9.7}Ag_3$ MG powders (ShanDong LianHong New Material Technology Co., Ltd China), with a nominal particle size ranging from 0 μm to 53 μm, were used in the L-PBF process for the specimen fabrication. The powder morphology was observed in scanning electron microscopy equipped with an energy disperse spectroscopy (SEM, Sigma 300, Zeiss, Germany) detector. Fig. 1a shows the spherical MG powders fabricated by the gas atomization process. The SEM results indicate that the powders exhibit good sphericity, uniform particle size, and high surface quality, meeting the requirements for L-PBF forming experiments. Table 1 presents the comparison between the nominal composition and actual composition of MG powders.

The MG specimens, including bulk and lattices, were manufactured using a selective laser melting system (SLM 125 HL, SLM Solutions Group AG, Germany). The system was equipped with a single 400W IPG fiber laser and operated under a continuous Argon

atmosphere. The oxygen content during the entire process was below 300 ppm. A zigzag scanning strategy with a 67° rotation was utilized in the subsequent layer building process, with a hatch distance of 100 μm. The laser scanning speed, laser power, and layer thickness were 1400 mm/s, 160W, and 60 μm, respectively.

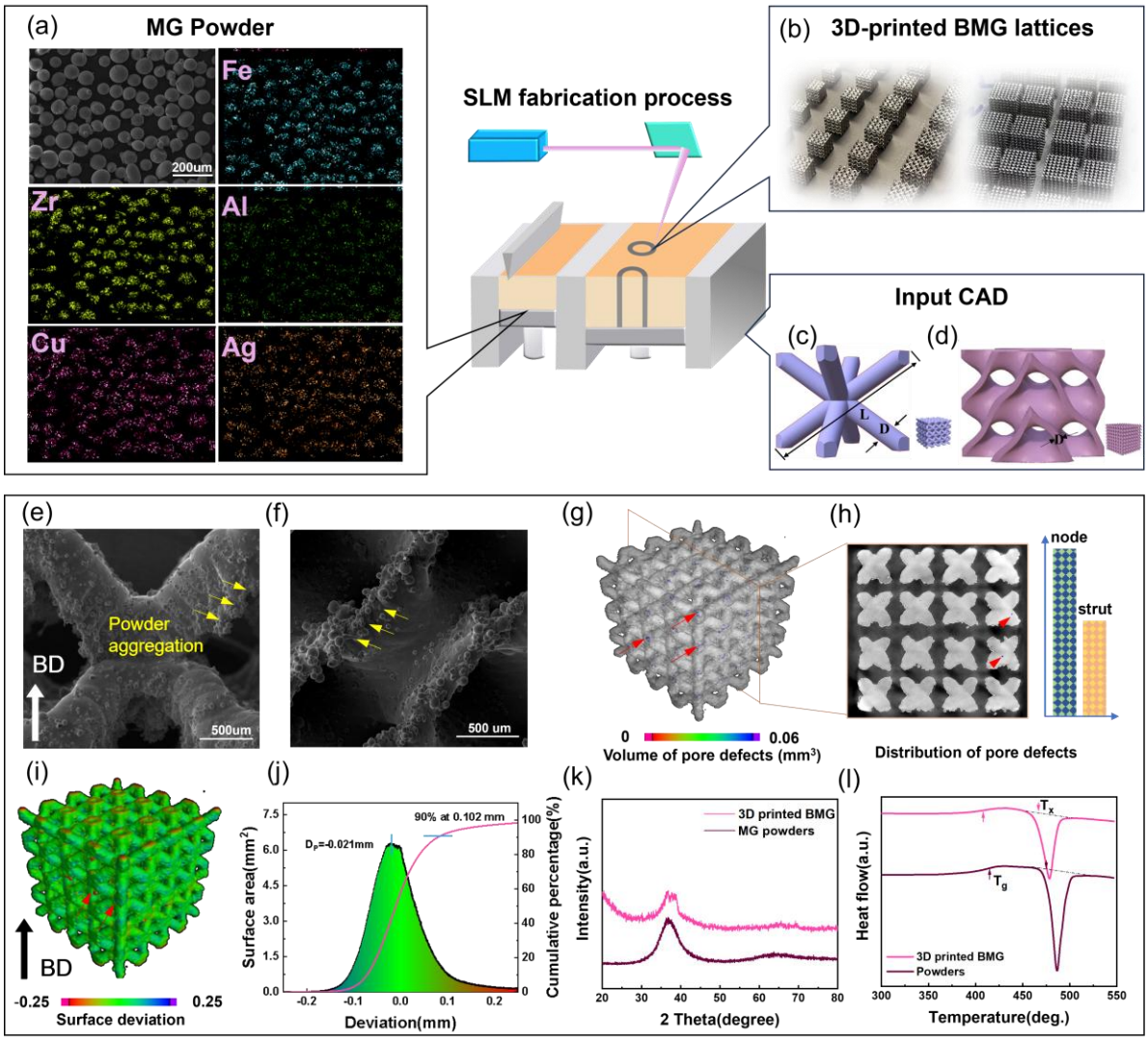

Fig. 1 The design, fabrication and characterization of the 3D-printed BMG lattices. (a) The morphology in SEM of $Zr_{60.14}Cu_{22.31}Fe_{4.85}Al_{9.7}Ag_3$ MG powder used in the SLM approach corresponding EDS element maps. (b) 3D-printed BMG specimens. CAD models of the unit cell of (c) BCC and (d) D-TPMS. SEM images of the outside surface of 3D-printed BMG lattices:(e) BCC and (f) D-TPMS. (g) Three-dimensional pores distribution of BCC BMG lattices and (h) data statistics of the number of pores distributed at nodes and struts. (i) Three-dimensional surface deviation maps and (j) statistical surface deviation distributions of BCC

BMG lattices (D_p was the peak surface deviation, 0.102 indicated the intercepts for 90% of the cumulative percentage.) (k) XRD patterns and (l) DSC plots of the 3D-printed BMG and MG powders, respectively.

Table 1 The comparison between the nominal and actual composition of powders

Composition	Zr	Cu	Fe	Al	Ag
Nominal (%)	60.14	22.31	4.85	9.7	3
Actual (%)	57.23	27.1	4.95	8.46	2.26

In this paper, we have selected a classical strut-based BCC lattice structure and a novel sheet-based D-TPMS structure for our initial attempt to integrate MG into cellular structures. Printed MG lattices shown in the Fig. 1b. COMSOL and Magics software were used to create 3D models and slice the 3D stereo-lithography (STL) files for 3D printing, as shown in Fig. 1c-d. The geometric properties of BCC are shown in Table S1. These four BCC structures (D0.8L2.8- D0.8L4.0) have cubic unit cells with decreasing side lengths so as to obtain diverse porosities (D and L refer to the diameter and the length of the structure of the unit cell). The TPMS structure's geometric model can be mathematically estimated through implicit methods[26]. This approach generates 3D surfaces as the solution of level set function Φ = c, referred to as the c-level set. The Diamond surfaces of the structure are described by the following approximations：

$$\Phi_D(x,y,z) = \sin(\omega x)\sin(\omega y)\sin(\omega z) + \cos(\omega x)\sin(\omega y)\sin(\omega z) + \sin(\omega x)\cos(\omega y)\sin(\omega z) + \sin(\omega x)\sin(\omega y)\cos(\omega z) = c \quad \text{Eq.1}$$

where x, y and z are spatial coordinates, $\omega = 2\pi/l$ and l is the length of a unit cell.

A 3D model of the TPMS sheet geometry (Fig. 1d) is created by extracting the zero-level surface from Eq. 1 in a MATLAB script, i.e., the surface defined by Φ = 0, and then offsetting the surface uniformly in both directions. The geometric properties of D-TPMS are shown in Table S1. These four TPMS structures have the same cubic unit cells with increasing shell thickness to obtain diverse decreasing porosities (T refers to the shell thickness). The porosity

of the TPMS was set consistent with the BCC lattices to have a better comparison.

2.2 Morphological and microstructure characterization of the 3D-printed BMG lattices

The structural features of the BMG lattices were characterized using FF35 X-ray computed tomography (CT, YXLON, Germany). The CT tests were conducted at a voltage of 150 kV and a current of 30 μA. To evaluate the densification level of the 3D-printed lattices, a representative BCC lattice structure with dimensions of 2.31×2.31×2.31 unit cells was scanned. Commercially available image analysis software, VG Studio Max 3.5 (Volume Graphics GmbH, Heidelberg, Germany), was employed for further data analysis and visualization.

For a more in-depth analysis of manufacturing deviations resulting from the fabrication process, the actual porosities of the printed lattices were determined using the dry weighing method. A wire-cut electrical discharge machining process was utilized to detach all specimens from the platform, and the wire-cut surfaces were subsequently mechanically polished with sandpaper. After drying, polishing, and cleaning, the samples were weighed. To calculate the total volume occupied by each lattice, all specimens were measured three times using a vernier caliper. The porosity *P* of the lattices was calculated as

$$P = \left(1 - \frac{\rho}{\rho_0}\right) \times 100\% \quad \text{Eq.2}$$

where ρ is the density of the structural alloys, ρ_0 is the densitiy of the bulk alloys.

The phases in the original MG powders and 3D-printed BMG lattices were investigated by X-ray diffractometer (XRD, Rigaku SmartLab 9KW, Japan) with a 2θ range from 20° to 80° and a differential scanning calorimeter (DSC 250, TA, USA) with a heating rate of 20K/min.

Compression tests were carried out on a 68TM-50 Universal testing machine (Max 50kN) (Instron, USA). Each test was performed under displacement control with a strain rate of 1.0 × 10^{-3} s^{-1} at room temperature and stopped when the entire structure completely collapsed. The loading direction was along the z-axis. Mechanical properties of 3D-printed BMG were tested in accordance with ASTM E9-09, where the compressive strength represents the maximum stress at or before fracture for brittle materials. The sample sizes of the BCC and TPMS lattices are provided in Table S1, and Table 3 indicates the geometrical specifications of

the BCT lattices.

2.3 Unit cell shape design on BCC structure to enhance the damage tolerance.

Since strut-based BMG lattices demonstrate a superior capacity to inhibit the expansion of impact-induced crack penetration through local fracture, we initially selected the BCC lattice as our baseline model. In the context of macro lattice structure design studies, the compressive deformation behavior of the meshes is influenced by the coupled mechanisms of bending and buckling. Drastic buckling behavior can be mitigated by increasing the bending component through unit cell shape design. Thus, to address the inherent brittleness of BMG during compressive deformation, unit cells are designed to increase the bending component of the load applied to the struts. These specially designed BCT structures (D0.8L3.2-90%- D0.8L3.2-70%) are derived from the cubic unit cell: D0.8L3.2, by scaling the unit cell in the z-axis direction using the corresponding multiplier α (ranging from 90% to 70%), as depicted in Fig. 5b. This method of altering the unit cell shape maintains consistent porosity across the entire mesh, facilitating meaningful comparisons of different unit cell shapes under the same volume fraction.

2.4 Finite element model of the designed BCC MG lattices

To elucidate the strengthening mechanism of the designed BCC BMG lattices, the linear finite-element (FE) quasi-static compression simulation was conducted to investigate the stress distribution by the commercial software COMSOL multiphysics. Mechanical properties of 3D-printed $Zr_{60.14}Cu_{22.31}Fe_{4.85}Al_{9.7}Ag_3$ for the FE method are illustrated in Fig. S1. We simulated experimental compression conditions by placing the BCC meshes between two rigid flat plates. The top plates were allowed to move only along the Z-axis, while the bottom plates were fixed in all directions. The model was meshed using free tetrahedral elements. To account for static friction between the plates and the samples, the frictional coefficient was set to 0.15.

205 **3. Results**

206 *3.1 Morphological characteristics and microstructure of the 3D-printed BMG lattices.*

207 Fig. 1 e-f illustrates the SEM images of 3D-printed BMG lattices characterized by low
208 roughness and a defect-free structure. However, it is noteworthy that some residual, unmelted
209 powder adhered to the outer surface, resulting in deviations between the measured and designed
210 porosity levels of the lattices.

211 3D-printed BCC specimens were quantitatively evaluated by the X-ray CT method (Fig. 1g-
212 j). From the defect volume distribution data presented in Fig. 1g, it is evident that the internal
213 pores within the fabricated lattice predominantly measure below 0.001 mm^2, resulting in a mere
214 0.06% defect volume ratio. This signifies that the sample's density exceeds 99.9%. We counted
215 the number of the pores distributed at the nodes and struts in Fig. 1h, which were 523 and 828,
216 respectively. The distribution histogram indicates that the pores are more likely to appear at the
217 nodes. The predominant green coloration within the contours in Fig. 1i-j denotes surface
218 deviations, which exhibit a commendable acceptability level, with 90% of deviations
219 measuring below 0.13 mm.

220

221 **Table 2 Geometrical characteristics of the as-designed lattices and mass comparison of**
222 **the as-built lattices and as-designed lattices**

Lattice sample code	Designed m_d (g)	Measured average m (g)	Deviation η_m (%)	Measured porosity (%)
D0.8L4.0	2.41	2.32 ± 0.03	3.88	59.5
D0.8L3.6	2.05	2.02 ± 0.01	1.49	52.1
D0.8L3.2	1.71	1.73 ± 0.08	1.16	42.6
D0.8L2.8	1.36	1.39 ± 0.04	2.16	30.6
T293	3.04	4.07± 0.01	25.3	41.3

T345	3.59	4.42± 0.02	18.78	35.8
T403	4.22	4.97± 0.01	15.09	28.0
T468	4.92	5.78± 0.01	14.88	16.1

223

224 Table 2 shows the dry weight of 3D-printed BMG lattices. Due to the different structures,
225 the measured average mass ranges from 2.32 g to 4.92 g, and porosities range from 59.5%-
226 16.1%. For the four BCC structures, the mass deviations: $\eta_m = \frac{|m_d - m|}{m} \times 100\%$, are below
227 4%. These deviations came from the error caused by the wire cutter and the powder aggregation
228 on the struts and nodes as shown in the SEM figures in Fig. 1e, which are acceptable results
229 for small dimensions lattices within 10 mm.

230 Mass deviations η_m in TPMS structures exceed 14%, which is influenced by various
231 factors due to their unique shell-based design. To efficiently design the geometries, TPMS
232 structures offer inherent advantages but require discretization into mesh models for additive
233 manufacturing. Enhanced calculation accuracy is essential. Despite the influence from the input
234 mesh model, the large melt pool size and over-melting during the fabrication process made the
235 residual particles more likely adhere to the surfaces; thus, the measured average weights m of
236 TPMS lattices are all bigger than the designed m_d. As the nominal thickness increases, the
237 volume fraction increases, while the deviation decreases. One of the primary reasons is that the
238 nominal thickness setting is too small compared to the laser spot size (80 μm). The overmelting
239 phenomenon significantly impacts the relative densities. As the nominal setting increases, the
240 effect of overmelting decreases, bringing m closer to the designed m_d. The nominal thickness
241 designed in this study is constrained by overall dimensions to maintain porosity consistent with
242 the BCC structures.

243 Fig. 1k-l shows the XRD and DSC results of the Zr-based MG powders and the 3D-printed
244 BMG. The XRD pattern of the powders exhibits a broad halo diffraction peak without any
245 detectable crystalline peaks, demonstrating a fully glassy structure. The 3D-printed BMG
246 exhibits a similar broad diffraction peak with small crystalline peaks on it, with the
247 nanocrystalline maybe induced during the 3D-printng process in the heat-affected zone (HAZ)

[27]. DSC results also indicate that there exists partial crystallization in the printed BMG. The amorphous content of the 3D-printed samples was determined using the equation $Am.\% = \Delta H/\Delta H_p$ [28], where $Am.\%$ represents the fraction of the amorphous phase, and ΔH and ΔH_p denote the crystallization enthalpies of the printed samples and the original amorphous powders, respectively. From the DSC results, it can be inferred that the amorphous content in 3D-printed BMG is 72.25%. Generally, the BMG has a smaller amorphous fraction than the porous MG because the 3D-printed lattice exhibits significantly larger molten pools due to less constraint in S regions.

3.2 Mechanical properties of 3D-printed BMG lattices.

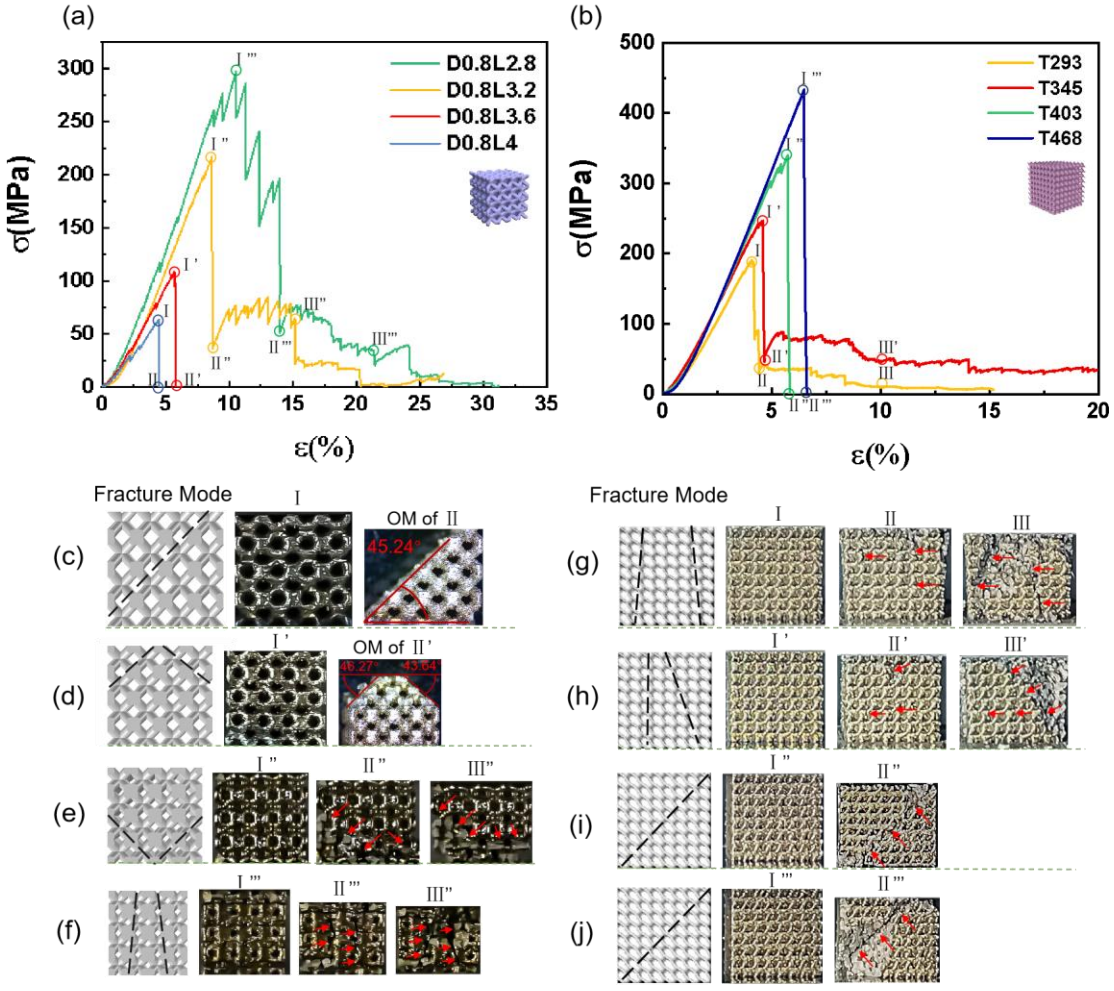

Fig. 2 Compressive stress-strain curves of 3D-printed BMGs with diverse porosities: (a) BCC lattices (b) TPMS lattices. Deformation behavior and fracture mode of diverse porosities

of BCC BMG lattices: (c) D0.8L4 (d) D0.8L3.6 (e) D0.8L3.2 and (f) D0.8L2.8 and TPMS BMG lattices (g) T293 (h) T345 (i) T403 (j) T468. The red arrow indicates the crack bands.

Fig. 2 displays the compressive stress-strain curves for BCC lattices and TPMS lattices with various porosities. For crystalline ductile metallic lattices, the stress-strain curves can be divided into three regions: an elastic deformation region before the first peak value is reached, a plateau region combining buckling and bending deformation, and a final densification region corresponding to rapid stress increase [29]. When it comes to MG lattices, their compression behavior is similar to that of brittle metallic lattices. The stress-strain curves of MG also exhibit three stages, as shown in Fig. 2a-b: an elastic deformation region before collapse strength σ_c (0- I), an extensive failure stage characterized by a dramatic drop in stress (I-II), a continuous local failure with decreasing low stress (II-III). Fig. 2c-j shows the deformations behavior and failure mechanisms of diverse porosities BCC lattices and TPMS lattices. For MG BCC lattices with high porosities (>50%), the compressive deformation behavior ends at stage II, with a single long fracture band throughout the whole structure due to catastrophic failure, leading to the stress suddenly dropping to 0 in the stress-strain curves (refer to I-II and I'-II' in Fig. 2c-d). The fracture angle measured from SEM figures is approximately 45°, consistent with the classical BCC lattice fracture mode. Furthermore, as the porosities decrease to less than 50%, the significant stress drop observed in stage II is reduced to a lesser extent. This behavior is clearer when the porosity decreases to 30.6% (specimen D0.8L2.8), at stage II (I"'-II"'), and this dramatic drop is manifested as a single significant reduction rather than multiple discontinuous drops. This corresponds to the propagation of multiple crack bands inside the structure (as shown in Fig. 2f), leading to the beam fracture at various locations until the entire structure collapses. The lower porosity introduced here corresponds to smaller pore sizes, which hinder the connection of crack bands under loading, thus preventing catastrophic failures. However, it remains challenging to completely avoid the dramatic stress drops in stage II by controlling pore size and porosity.

Unlike BCC structures that consist of struts and nodes, TPMS structures lack nodes, which

reduces stress concentrations. From previous FE results of the Diamond TPMS structure [24], sheet-based structures exhibit a homogeneous failing manner, where all layers demonstrate relatively uniform deformations under applied loads. However, due to the brittle materials characteristics, TPMS MG lattices did not behave better than BCC structures as expected. They exhibit high strength but with catastrophic failure under compression. At porosities higher than 30%, multiple cracks rapidly propagate the structures in the loading direction. In Fig. 2g-h, we can clearly see that the crack bands separate the lattices into several parts. However, since the crack propagation direction is parallel to the loading direction, the lattices can maintain structural integrity for a while to bear the load in the Z direction. However, due to severe damage, the load-bearing capacity is maintained at low-stress levels with a continued detachment of the broken parts from the structure. When the porosity decreases below 30%, the crack band becomes singular, and the fracture angle is 45% (Fig. 2i-j). As the porosity decreases, the fracture mode of the TPMS MG lattices is contrary to that of the BCC MG lattices. Compared with the sheet-based structure TPMS, more stress fluctuations occur on strut-based BCC structure, and localized fracture of the struts absorbs the compression energy, thus avoiding primary crack generation and rapid penetration throughout the sample.

In summary, when the loading stress exceeds the elastic limit of the brittle material, these artificially introduced porous structures dissipate the input energy by proliferating microcracks as the applied strain increases. As the energy in the material is dissipated and the stress is relaxed, there is no main crack penetration. This is the result of quasi-static loading of the porous structure to enhance the deformability and damage resistance of brittle materials.

3.3 Ashby predicted model.

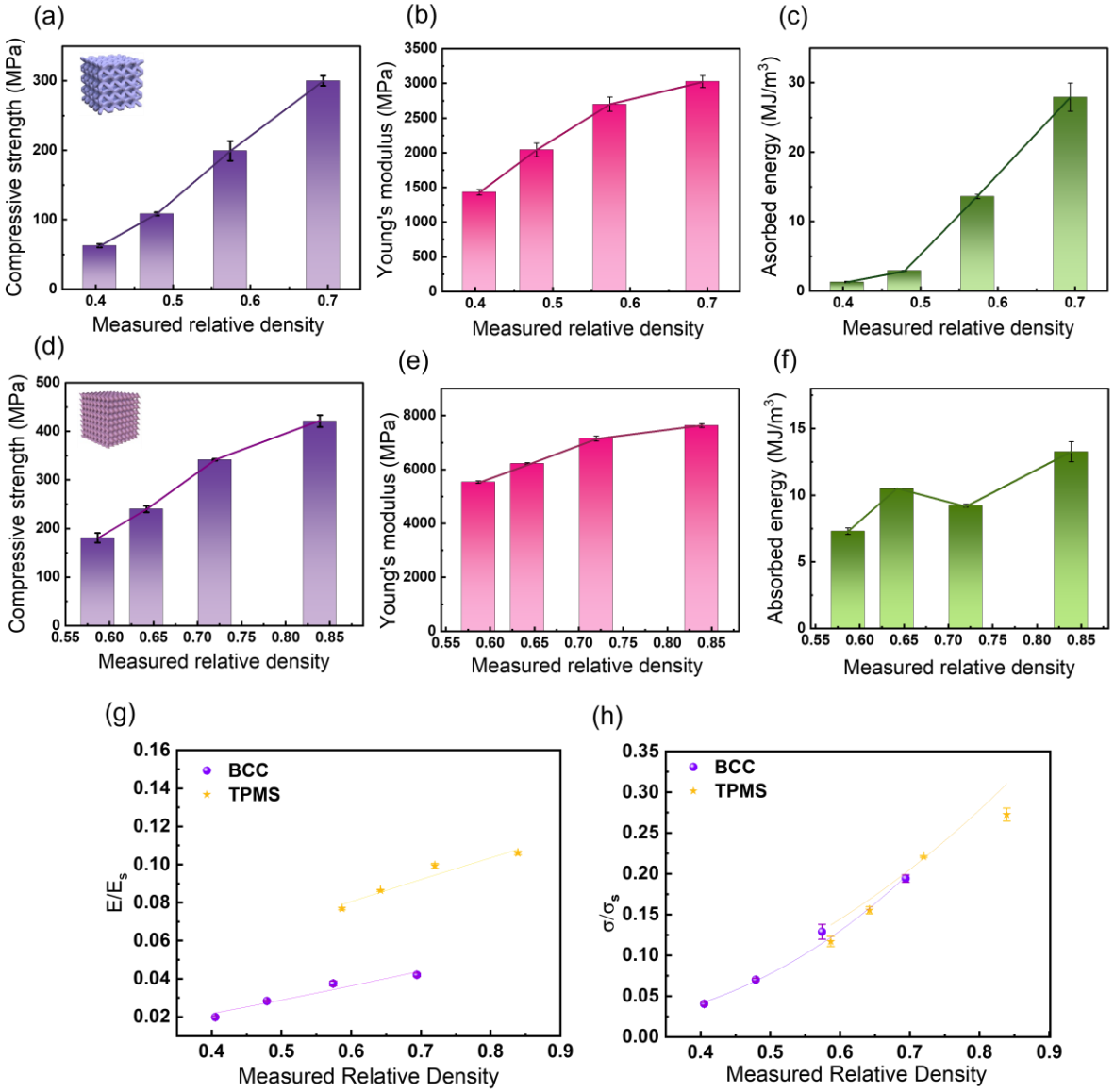

Fig. 3 Mechanical properties of BCC BMG lattices (a-c) and TPMS BMG lattices (d-f): Compressive strength, Young's modulus, Energy absorption versus the measured relative density. Comparison on (g) normalized elastic modulus (h) normalized compressive strength.

Variations in compressive strength σ, Young's modulus E, and energy absorption W with measured porosities of two types of lattices are shown in Fig. 3a-c for BCC lattices and Fig. 3d-f for TPMS lattices. The strength ranges from 50 MPa to 300 MPa for BCC lattices and 150 MPa to 450 MPa for TPMS lattices. Young's modulus E ranges from 1.0 to 3.0 GPa for BCC

lattices, and from 5.0 to 8.0 GPa for TPMS lattices. Energy absorption capacity, namely the amount of energy absorbed per unit volume of cellular solids, is determined by the area under the stress-strain curve up to the densification strain:

$$W = \int_0^{\varepsilon_c} \sigma(\varepsilon) d\varepsilon \quad \text{Eq.3}$$

Since the BMG in this study is extremely brittle, the collapse strain ε_c (point III in Fig. 2) is used instead of the densification strain. If BMG lattices cause catastrophic failure and do not have stage III, only the former two stages are considered to calculate the energy absorption. Energy absorption requires an optimum combination of large collapse strain and high plateau stress. Thus, for the brittle foams, avoiding the abrupt stress drop at stage II and extending the plateau region at stage III is vital for enhancing the energy absorption ability.

Based on the classic theory of cellular solids, the structure-property relationship of different unit cell MG lattices can be established. The normalized compressive strength σ and the normalized elastic modulus E of the porous structure can be represented as a function of relative density by power laws [30, 31]:

$$\frac{E}{E_S} = C_1 \bar{\rho}^{n_1} \quad \text{Eq.4}$$

$$\frac{\sigma}{\sigma_s} = C_2 \bar{\rho}^{n_2} \quad \text{Eq.5}$$

Where σ and E_s are the compressive strength and Young's modulus of the raw material, Zr-based BMG (Fig S1). The exponents n_1, n_2, along with the coefficients C_1, C_2, serve to characterize the mechanical properties of the distinct geometries of unit cells, and the exponents are more representative since they follow power laws. It is important to note that the relative densities of the lattices in this work are measured densities, not nominal relative densities. Many previous investigations have used the nominal relative density to establish the structure-property relationship, but greater precision is necessary, especially when manufacturing errors are significant and must be taken into account. It also lacks persuasiveness when compared with other cellular materials in terms of nominal relative density, particularly for specimens with significant fabrication deviations [32].

Fig. 3g-h shows the normalized elastic modulus and normalized compressive strength. In

this study, the mechanical properties along the <100> direction are calculated because of the anisotropy of lattice structures. For the normalized elastic modulus, the fitting exponent of the TPMS structure is 0.872, which is smaller than that of the bending-dominated BCC lattices (1.26). The fitting exponents are obtained from the nonlinear curve fitting results based on Eq.4 and Eq.5. The small exponent of the TPMS structure means that the compressive modulus decreases were slowly with decreased density compared to the BCC lattice, amplifying the advantage in the low-density range. As an example, based on the fitting equations in Fig. 3g, Young's modulus of the TPMS structure is 2.05 times that of the BCC lattice at a relative density of about 0.58. Similar experimental results in previous literature indicated that the TPMS structure outperforms BCC lattices in regard to the modulus [24]. However, unlike most BCC lattices with exponents greater than 2, the BCC MG lattice in this study has a much lower exponent than in previous works. This suggests that BCC structures perform better on BMG than expected. For compressive strength (Fig. 3h), the fitting exponent of the TPMS structure is 2.28, which is also slighter smaller than for BCC lattices (2.84). At approximately the same relative density of 0.58, BCC BMG lattices even exhibit slightly higher compressive strength than TPMS BMG lattices. This result contrasts with findings in other works on ductile materials, such as 316L stainless steel and maraging steel [24, 33, 34]. Modest stress fluctuations occur during the elastic stage (Stage I) of BCC MG lattices in Fig. 2, indicating that some small parts of the struts fracture inside the lattices to release the stress. This allows the entire lattice to bear more loading until it fails. In contrast, TPMS structures with smoother surfaces are less prone to break at stress concentration points for releasing internal energy. As a result, their stress curves form straight lines without fluctuations during the elastic stage.

The above experimental phenomena indicate that for brittle materials, the optimum and suitable structure is different due to the different failure mechanism and materials characteristics; hence, the structure design strategy cannot follow that of ductile cellular materials. A novel design method should be developed based on the compression experimental results of BMG lattices, considering the failure characteristics of brittle materials.

3.4 Enhanced damage tolerance of designed unit cell shape BMG lattices.

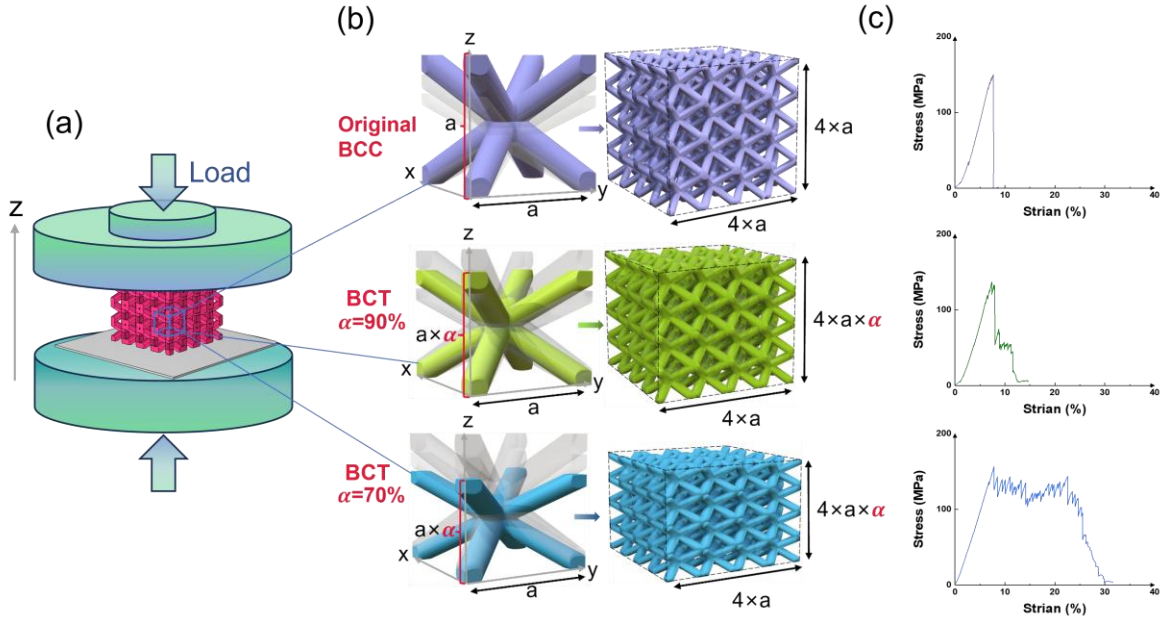

Fig. 4 Schematics of unit cell shape design strategy. (a) compression test and load direction (b) BCC unit cell shape design: the original BCC lattice and BCT-90%, BCT-70%. (c) The enhancement of damage tolerance of designed lattices.

It was found that the deformation characteristics mainly depend on the geometries of the unit cell rather than the relative density. In this study, the unit cell design is based on the original BCC structure (D0.8L3.2). The BCC unit cell was transformed into a BCT unit cell, being compressed in the z-direction to different degrees. α represents the scaling degree in the z-direction. Detailed geometrical information for the BCT lattices is provided in Table 3. Visible enhancements in the damage tolerance were investigated through the stress-stain curves with increasing multiplier α in Fig. 4c.

390 **Table 3**

391 **Geometrical specifications of the BCT lattices**

Lattice sample code	Unit cell size (mm)	Number of cells (x,y,z)	Angles between the applied load and the beam (°)	Measured porosity (%)
D0.8L3.2-90%	1.85 × 1.85 × 1.66	(4,4,4)	32.47	40.8
D0.8L3.2-85%	1.85 × 1.85 × 1.57	(4,4,4)	31.01	39.2
D0.8L3.2-80%	1.85 × 1.85 × 1.48	(4,4,4)	29.50	39.6
D0.8L3.2-70%	1.85 × 1.85 × 1.29	(4,4,4)	26.33	39.4

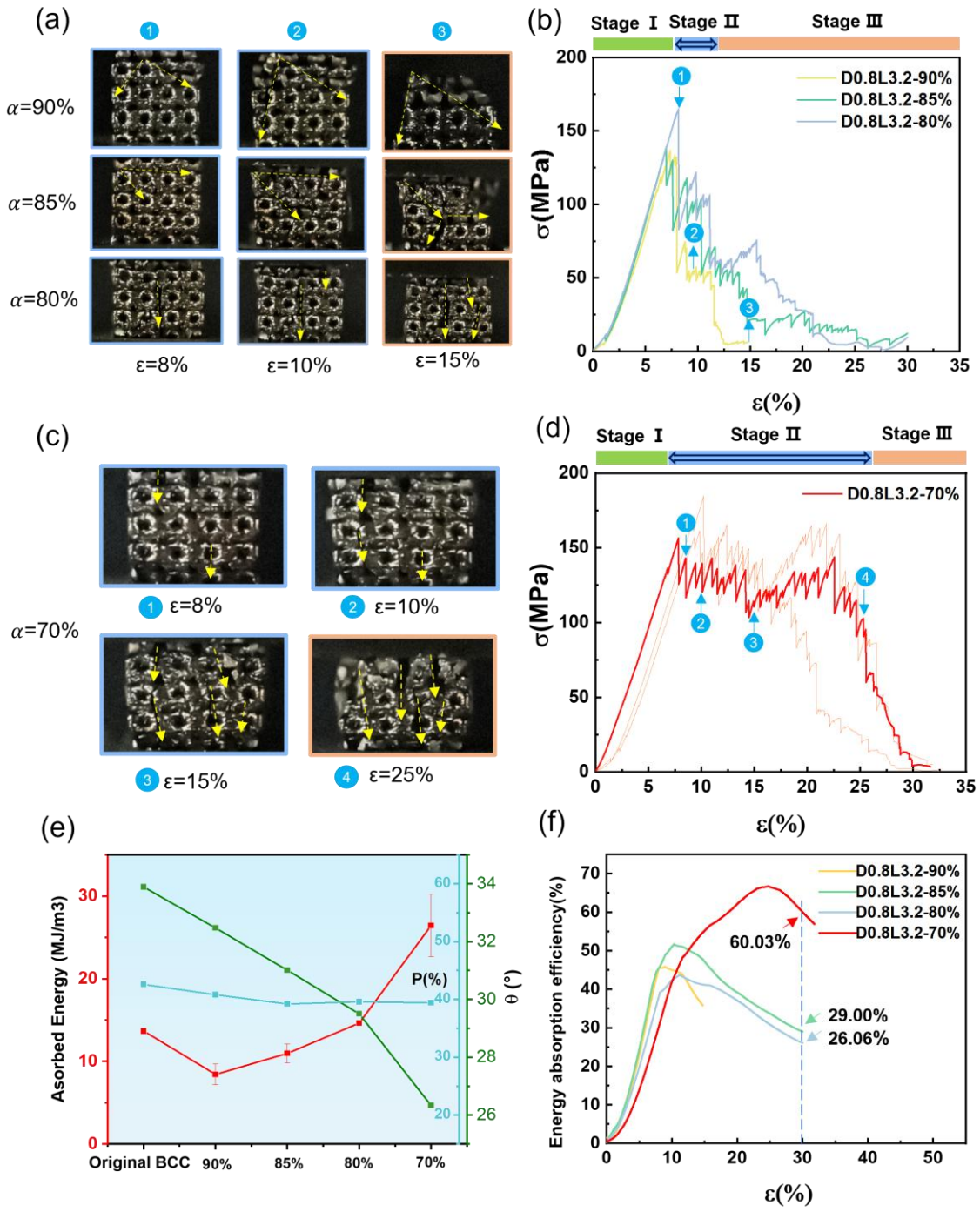

Fig. 5 Mechanical performance of designed BCT lattices. (a) Deformation process and (b) stress-strain curves of the designed BCT lattices with slight scaling degree: D0.8L3.2-90%, D0.8L3.2-85% and D0.8L3.2-80%. (c) Deformation process and (d) stress-strain curves of the BCT lattices with a large scaling degree: D0.8L3.2-70%. Increasing energy absorption performance with the increased scaling degree of the lattices(e) Absorbed Energy (f) Energy absorption efficiency.

From the compression results and deformation phenomenon in Fig. 5a-b and Fig. 5c-d, a clear transition from catastrophic fracture to sequential localized fracture was observed with the scaling degree. For the BCT structure with a slight scaling degree ($\alpha = 90\%$), the stress drops to 50 MPa immediately after the compressive strength σ reached 136 MPa (Fig. 5b). Two main cracks could be seen in the deformation process (Fig. 5a) at ε =10%. Two cracks propagated rapidly and divided the lattices into several big parts that no longer bear any stress at ε =15%. In Fig. 5d, the designed BCT structure with a large scaling degree ($\alpha = 70\%$) displays an enhanced stress level after the elastic deformation region, which is close to the plateau region of the ductile metallic lattices. Multiple small crack bands occur but no main crack bands through the entire lattices; thus, no rapid stress drop at stage II after lattices reach the compressive strength σ of 156 MPa. At stage II-III, the stress fluctuates from 100 to 140 MPa for a strain rate of approximately 17.7%, corresponding to the continuous crushing of the struts. The direction of the crack bands is along the loading direction, thereby maintaining a high-stress level in a long region. The rapid stress drop was postponed significantly, and the whole lattices still maintained 102 MPa at ε =25%.

To absorb more energy when compressed, ideal absorption materials had a long plateau. The absorbing ability of porous structures is demonstrated solely by W. The energy absorption efficiency, denoted as η, serves as an indicator of the energy absorption capacity of engineered lattice structures, relative to the product of the maximum stress $\boldsymbol{\sigma}$ and strain. The value of η can be calculated by[35]:

$$\eta = \frac{W}{\sigma\varepsilon} \quad \text{Eq. 6}$$

The BCT lattice possesses a greater energy absorption capability, resulting from its unique mechanical deformation behavior, compared to the original BCC structure. The absorbed energies of the fabricated BCT MG lattices gradually increased with decreasing angles θ between the applied load and the beam. From Fig. 5e, the absorbed energy of the original BCC (θ = 33.89 °) is 13.67 MJ/ mm^3. As the angle θ of the unit cell decreases to 26.33°, the absorbed energy of the BCT lattice is 29.25 MJ/ mm^3 (almost 2.2 times that of the original BCC). The energy absorption efficiencies of the fabricated different BCT MG lattices (Fig. 5f)

427 with 30% strain are 26.06%, 29.00, and 60.03%, respectively. The results also indicate that the
428 unit cell shape design has a significant positive influence on the absorption efficiencies of 3D-
429 printed BMG lattices, attributable to the high-stress level in the plateau region. Especially for
430 D0.8L3.2-70%, the energy absorption efficiency at 30% is close to the highest energy
431 absorption efficiencies of the amorphous metal nano-honeycomb (70%-90%) [36] and is higher
432 than that of the open-cell lattice structure (50%) [35].

4. Discussion

4.1 Principles to improve the damage tolerance of BMG lattices through unit cell shape design.

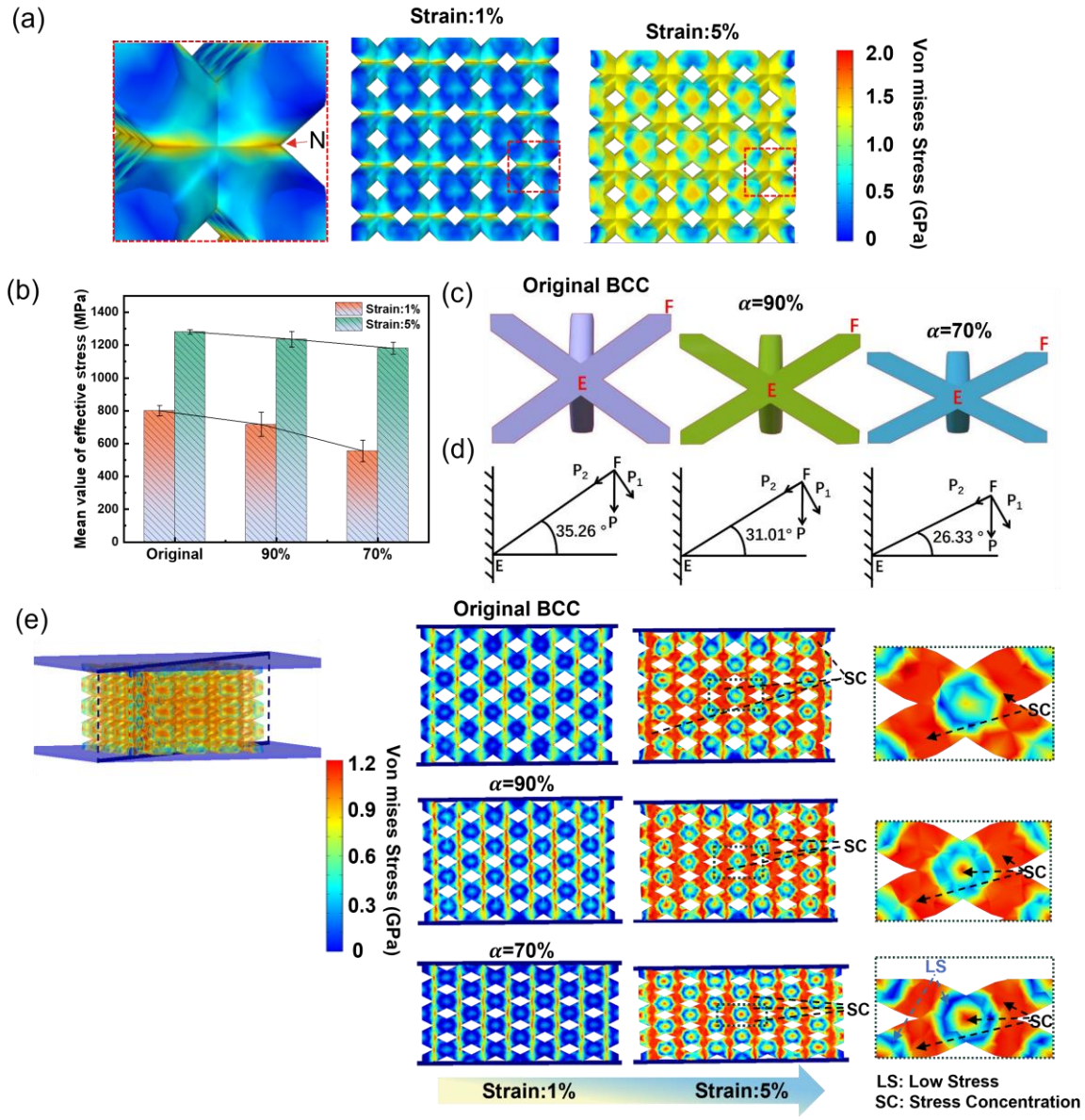

Fig. 6 Stress analyses of the designed BCC lattices. (a) FE predicted stress distributions at different strains for BCC lattices. (b) Mean value of equivalent stress of N point of the BCC lattice and BCT lattices at 1% and 5% overall deformation. (c) Orthogonal cross-section and (d) Force analysis diagram of the BCC unit cell and the BCT unit cell with different scaling degrees: D0.8L3.2, D0.8L3.2-90% and D0.8L3.2-70%. (e) FE predicted stress distributions

441 (orthogonal cross-section) at different strains for the BCC lattice and BCT lattices: D0.8L3.2,
442 D0.8L3.2-90% and D0.8L3.2-70%.

443 Clear enhancement in the damage tolerance of the BCT lattices (Fig. 5) was observed from
444 the compression results and deformation phenomena in the deformed unit cell. In this section,
445 theoretical analysis is used to elucidate the factors behind this transformation. To precisely
446 evaluate the mechanical properties like collapse strength and elastic modulus through geometry
447 information of unit cells and the intrinsic properties of raw material, a basic model was formed
448 based on those deformation modes [37, 38]. To better understand the influence of the designed
449 structure on mechanical behavior, the load P applied on a z-axis strut is separated by two
450 components P_1 and P_2, where P_1 represents the load along the bending direction (Fig. 6c-d),
451 and P_2 represents the load along the buckling direction. Obviously, P_2 decreases with
452 decreasing θ of the unit cell, whilst on the contrary, the bending component P_1 increases. This
453 tendency is consistent with the other material lattices deformation behaviors under compression
454 [25].

455 However, a different mechanism is at play when dealing with brittle BMG. The increased
456 force P_1 induces vertical fracture at various positions inside the lattices, while the decreased
457 force P_2 reduces the stress concentration in the direction of the diagonal, avoiding the fast
458 propagation of the main crack bands. This point is substantiated by the numerical results
459 obtained from finite element analysis. From the linear-elastic simulation models in Fig. 6a, the
460 stress is concentrated on the nodes (N point) of the BCC lattices. The lower mean value of the
461 equivalent stress at point N in the BCT lattices at 1% and 5% overall deformation (elastic stage).
462 Fig. 6b indicates that the D0.8L3.2-70% lattices have lower stress concentration at the N point,
463 consistent with the decrease in the component P_2. The reasons for the transition of this fracture
464 mode can be intuitively determined from the orthogonal cross-section of the stress distribution
465 results in Fig. 6e. It was found that the maximum von Mises stresses observed in the original
466 BCC unit cell were distributed nearby the nodes but formed localized high-stress bands along
467 the diagonal line. With the decrease of the component P_2, higher amounts of high-stress
468 distribution were concentrated in the struts rather than the nodes. Low-stress areas were

presented between the nodes and struts in the D0.8L3.2-70% lattices, acting like a wall that blocks the rapid propagation of cracks along the diagonal direction. Hence, multiple crack bands along the vertical direction appeared instead of a single crack band along the diagonal.

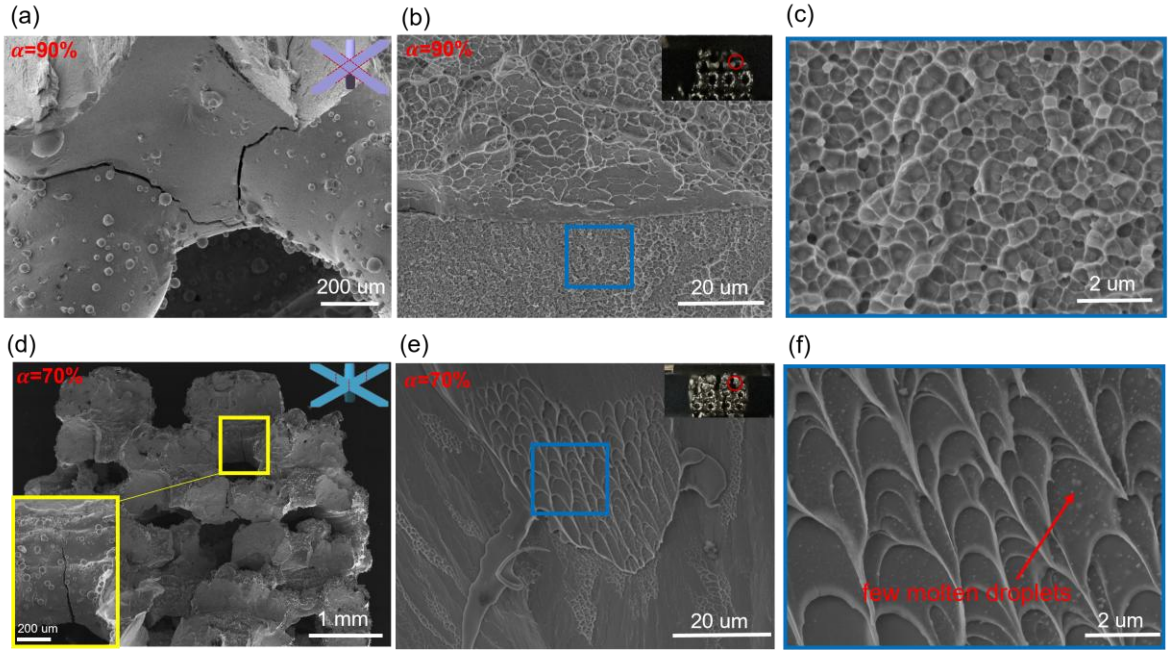

Fig. 7 Crack surface and fractography of designed BCC BMG lattices. SEM images of exemplary compression test sample after crack initiation: (a)D0.8L3.2-90%: crack propagate along the diagonal line (b-c) fracture morphologies: dimple-like pattern. (d) D0.8L3.2-70%: crack propagate along the vertical direction (e-f) fracture morphologies: vein-like pattern.

The transformative crack extending behavior of the BCT lattice can be investigated from the fracture surface of the lattices. As shown in Fig. 7a, the trajectories of the cracks follow the junctions between the nodes and struts, which are areas of high von Mises stress, and propagate rapidly along the diagonal direction throughout the entire lattice. In D0.8L3.2-90% lattices with larger θ, the fracture surface displays a dimple-like pattern (Fig. 7b-c), a typical feature of quasi-cleavage brittle fracture in MGs. For D0.8L3.2-70% lattices with the smallest θ (Fig. 7d), since there is a low-stress area between the nodes and struts, cracks no longer extend along the diagonal direction. Instead, they deflect along the vertical direction and are restricted by the porosities, preventing them from propagating throughout the entire structure. In addition, a

typical fracture (Fig. 7e-f) of the molten pool region of MG was observed. Many molten droplets were observed in the vein-like structure, demonstrating that concentration of elastic energy causes temperature increase over the T_g of the MG, while the energy is released in instantaneous fracture, and localized remelting occurs. This indicates that the deformation behavior of original BCC lattices is just fast crack propagation along the crack band compared to the BCT lattices with smaller θ. When the θ decreases, multiple small crack bands cause incompleteness of the structures with the complex stress distribution, and the struts make it easier to achieve the elastic limit that causes localized remelting of MP, which bears more loading. This result verifies the increased stress level at the plateau region.

4.2 Applying the present enhancement strategy in the future.

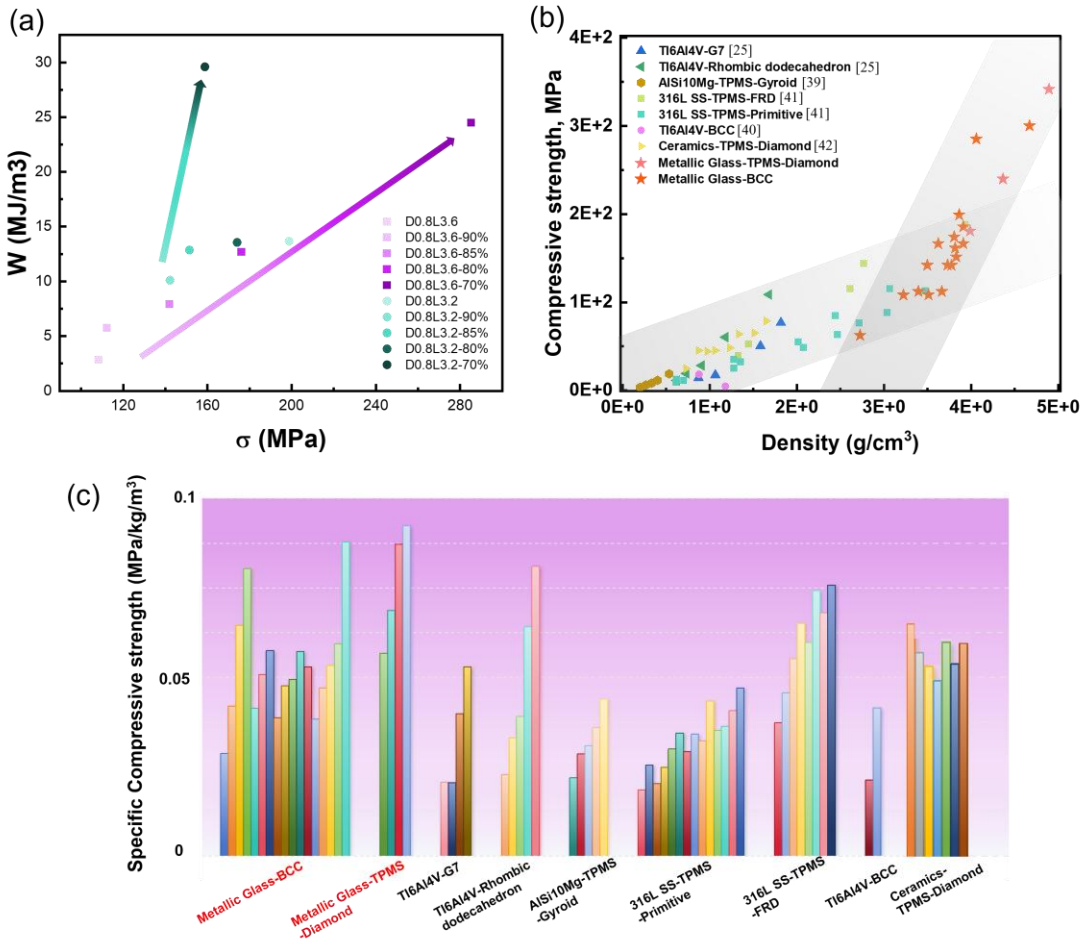

Fig. 8 Primary results on applying the present strategy to BCC BMG meshes. (a) the

energy absorption capacity against compressive strength: the arrow points in the direction of θ reduction. (b-c) compressive strength and specific compressive strength comparing the mechanical properties of MG meshes with other cellular structures [25, 39-42].

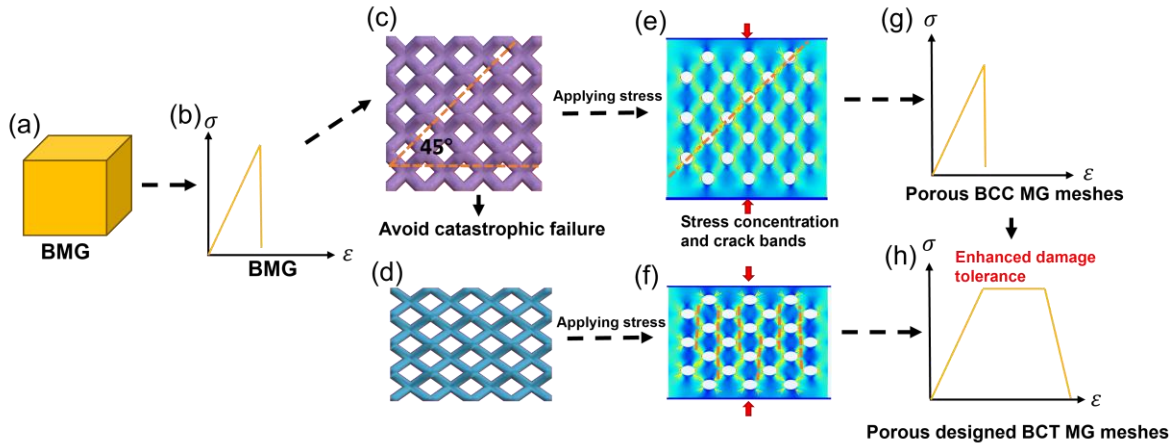

Fig. 9 An instance of implementing the present strategy for future lattice design to achieve improved mechanical performance. The introduced porosity based on original BCC lattices (c) is hard to effectively inhibit the intrinsic single crack band of BMG meshes (e, g). Designed BCT BMG meshes (d) with multiple crack bands (f) to achieve a better performance (h).

This work is the first attempt to combine the lattice structures with BMGs to achieve high damage tolerance of brittle structural materials with high strength. By the introduction of the designed unit cell with almost constant porosity, appreciable enhancement of the mechanical properties can be well obtained.

To verify the viability of the present strategy, we also designed the same shape for BCC lattices with different strut lengths and then measured the mechanical properties of 3D-printed BMG lattices under compression. Fig. 8a exhibits the active influence on both absorption energy capacity and compressive strength on BCC lattices with different strut lengths. The scatter with the darker color represents the BCT lattices with smaller θ. The compressive strength of the original BCC lattice (D0.8L3.6) is 108MPa, and when the deform multiplier α =70%, the compressive strength increase to 285 MPa. The absorbed energy also increased by 8.5 times, which is a significant improvement. For the D0.8L3.2 BCC structure, we can see that there is a positive effect on the energy absorption capacity with the increasing deform

multiplier α. Thus, establishing an accurate structure-property relationship for the present structure strategy based on different unit cells is essential to synergistically enhance the compressive strength and damage tolerance for meeting the high-performance requirements for energy absorber applications. In comparison with other cellular structures (Fig. 8b-c), BMG lattices exhibit outstanding strength-to-weight ratios, which shows the potential comparable ability of the MG lattices for the high strength need in the automobile and aerospace industries.

The schematic approach, which applies the current strategy for designing strut-based lattices, is depicted in Fig. 9. At room temperature, brittle BMGs have zero compressive plasticity (Fig. 9a-b). The complex BCC lattices can be simplified as 2D BMGs with artificial holes (Fig. 9e-f). Through unit cell design, the distribution of the high-stress bands can prevent the 45° main crack band under compressive loading, which leads to catastrophic failure (Fig. 9e). After unit cell design, micro cracks do not easily penetrate the neighboring pores and the linkage between the main crack and the microcracks can be avoided, and multiple small vertical crack bands occur which postpone the catastrophic failure (Fig. 9f). Small region fracture releases the energy concentration, the stress concentration is relaxed, and the stress state becomes complex with the variation of the lattices, thus improving the failure resistance of brittle BMG meshes. This design method can simultaneously improve compressive strength and damage tolerance. However, the structural anisotropy induced by this strategy leads to its limitations, as it can only improve the damage tolerance of unidirectional lattice structures.

5.Conclusions

To sum up, BMG meshes with BCC and TPMS cells were printed using the L-PBF method. It was found that the deformation behavior of these lattices can be summarized into three stages: an elastic deformation region before collapse strength, an extensive failure stage characterized by a dramatic drop in stress, and continuous localized fracture with a decreasing low stress. Unexpectedly, the BCC structures outperform TPMS structures in terms of absorption energy because the multiple fractures of the struts release partial energy, thereby postponing the

collapse of the structures. This result suggests that BCC lattice may be more suitable for highly brittle materials than TPMS structure to prevent the fast propagation of the main crack band, causing catastrophic failure.

Based on the influencing effects of the deformed BCC unit cell shape on the compressive deformation behavior, BCT lattices with increased multiple cracks were designed to enhance the damage tolerance of the lattices effectively. The catastrophic failure of the MG lattices was avoided by inducing localized fracture through reducing the angle θ of the unit cell. Compression test results showed that BCT BMG lattices have a positive impact on both absorption energy capacity and compressive strength. By employing this design strategy on the BCC MG meshes with different strut lengths, the energy absorption of the designed BCT lattices increased by nearly 8.5 times compared to the original BCC lattices. Simultaneously, the compressive strength increased synergistically by about 2.5 times. These results confirm that our method is effective in mitigating the catastrophic failure of brittle BMGs and enhancing the fracture behavior of BMG lattice structures, demonstrating their high potential for high-strength absorber applications.

CRediT authorship contribution statement

Congrui Yang: Conceptualization, Methodology, Software, Data Curation, Visualization, Investigation, Writing – original draft. **Di Ouyang**: Conceptualization, Validation, Investigation, Writing – review & editing. **Lei Zhang**: Conceptualization, Investigation, Writing – review & editing. **Yongyun Zhang**: Methodology, Writing – review & editing. **Xing**

Tong: Methodology, Writing – review & editing. **Haibo Ke**: Funding acquisition, Project administration, Methodology, Writing – review & editing, Supervision. **Kang Cheung Chan**: Conceptualization, Funding acquisition, Project administration, Writing – review & editing, Supervision. **Weihua Wang:** Funding acquisition, Project administration, Writing – review & editing, Supervision

Declaration of Competing Interest

The authors declare they have no conflict of interest.

Acknowledgements

The work was supported by Guangdong Major Project of Basic and Applied Basic Research, China (Grant No. 2019B030302010), the National Natural Science Foundation of China (No. 52201181, 52071222, 52001219), the National Postdoctoral Science Foundation of China (No. 2023T160240 and No. 2020M672336), and the National Key Research and Development Program of China (Grant No. 2021YFA0716302). The authors are grateful to Materials Research Centre in The Hong Kong Polytechnic University for their technical assistance.

References

[1] S.R. Hirshorn, NASA SYSTEMS ENGINEERING HANDBOOK, 2007,

[2] W. Wang, C. Dong, C. Shek, Bulk metallic glasses, Materials Science and Engineering R: Reports. 44(2-3) (2004) 45-89, https://doi.org/10.1016/j.mser.2004.03.001.

[3] B.T. Lee, S.K. Sarkar, Fabrication of super-high-strength microchanneled Al2O3–ZrO2 ceramic composites with fibrous microstructure, Scripta Materialia. 61(7) (2009) 686-689, https://doi.org/10.1016/j.scriptamat.2009.05.047.

[4] J. Wang, R. Li, N. Hua, T. Zhang, Co-based ternary bulk metallic glasses with ultrahigh strength and plasticity, Journal of Materials Research. 26 (2011) 2072-2079, https://doi.org/10.1557/jmr.2011.187.

[5] M. Telford, The case for bulk metallic glass, Mater Today. 7(3) (2004) 36-43, https://doi.org/10.1016/S1369-7021(04)00124-5.

[6] H.X. Li, Z.C. Lu, S.L. Wang, Y. Wu, Z.P. Lu, Fe-based bulk metallic glasses: Glass formation, fabrication, properties and applications, Progress in Materials Science. 103 (2019) 235-318, https://doi.org/10.1016/j.pmatsci.2019.01.003.

[7] J. Farmer, J.-S. Choi, C. Saw, J. Haslam, D. Day, P. Hailey, T. Lian, R. Rebak, J.H. Perepezko, J. Payer, D. Branagan, B. Beardsley, A. D'amato, L. Aprigliano, Iron-Based Amorphous Metals: High-Performance Corrosion-Resistant Material Development, Metallurgical and Materials Transactions A. 40 (2009) 1289-1305, https://doi.org/10.1007/s11661-008-9779-8.

[8] M. Davidson, S. Roberts, G. Castro, R.P. Dillon, A. Kunz, H. Kozachkov, M.D. Demetriou, W.L. Johnson, S. Nutt, D.C. Hofmann, Investigating Amorphous Metal Composite Architectures as Spacecraft Shielding, Advanced Engineering Materials. 15(1-2) (2013) 27-33, https://doi.org/10.1002/adem.201200313.

[9] N. Nishiyama, K. Takenaka, H. Miura, N. Saidoh, Y. Zeng, A. Inoue, The world's biggest glassy alloy ever made, Intermetallics. 30 (2012) 19-24, https://doi.org/10.1016/j.intermet.2012.03.020.

[10] W.H. Wang, Roles of minor additions in formation and properties of bulk metallic glasses, Progress in Materials Science. 52(4) (2007) 540-596, https://doi.org/10.1016/j.pmatsci.2006.07.003.

[11] J. Qiao, H. Jia, P.K. Liaw, Metallic glass matrix composites, Materials Science and Engineering: R: Reports. 100 (2016) 1-69, https://doi.org/10.1016/j.mser.2015.12.001.

[12] M.J. Duarte, J. Klemm, S.O. Klemm, K.J.J. Mayrhofer, M. Stratmann, S. Borodin, A.H. Romero, M. Madinehei, D. Crespo, J. Serrano, S.S.A. Gerstl, P.P. Choi, D. Raabe, F.U. Renner, Element-Resolved Corrosion Analysis of Stainless-Type Glass-Forming Steels, Science. 341(6144) (2013) 372-376, doi:10.1126/science.1230081.

[13] M.-X. Li, S.-F. Zhao, Z. Lu, A. Hirata, P. Wen, H.-Y. Bai, M. Chen, J. Schroers, Y. Liu, W.-H. Wang, High-temperature bulk metallic glasses developed by combinatorial methods, Nature. 569(7754) (2019) 99-103, 10.1038/s41586-019-1145-z.

[14] C. Zhang, X.-m. Li, S.-Q. Liu, H. Liu, L.-J. Yu, L. Liu, 3D printing of Zr-based bulk

628 metallic glasses and components for potential biomedical applications, J Alloy Compd. 790
629 (2019) 963-973, https://doi.org/10.1016/j.jallcom.2019.03.275.
630 [15] C. Yang, C. Zhang, W. Xing, L. Liu, 3D printing of Zr-based bulk metallic glasses with
631 complex geometries and enhanced catalytic properties, Intermetallics. 94 (2018) 22-28,
632 https://doi.org/10.1016/j.intermet.2017.12.018.
633 [16] P. Bordeenithikasem, Y. Shen, H.-L. Tsai, D.C. Hofmann, Enhanced mechanical
634 properties of additively manufactured bulk metallic glasses produced through laser foil
635 printing from continuous sheetmetal feedstock, Additive Manufacturing. 19 (2018) 95-103,
636 https://doi.org/10.1016/j.addma.2017.11.010.
637 [17] S. Chen, H. Cheng, K. Chan, G. Wang, Metallic glass structures for mechanical-energy-
638 dissipation purpose: a review, Metals. 8(9) (2018) 689, https://doi.org/10.3390/met8090689.
639 [18] R. Liontas, J.R. Greer, 3D nano-architected metallic glass: Size effect suppresses
640 catastrophic failure, Acta Materialia. 133 (2017) 393-407,
641 [19] C. Zhang, D. Ouyang, S. Pauly, L. Liu, 3D printing of bulk metallic glasses, Materials
642 Science and Engineering: R: Reports. 145 (2021) 100625,
643 https://doi.org/10.1016/j.mser.2021.100625.
644 [20] D. Ouyang, P. Zhang, C. Zhang, L. Liu, Understanding of crystallization behaviors in
645 laser 3D printing of bulk metallic glasses, Applied Materials Today. 23 (2021) 100988,
646 https://doi.org/10.1016/j.apmt.2021.100988.
647 [21] P. Zhang, C. Zhang, L. Liu, Toughening 3D-printed Zr-based bulk metallic glass via
648 synergistic defects engineering, Materials Research Letters. 10(6) (2022) 377-384,
649 https://doi.org/10.1080/21663831.2022.2054291.
650 [22] A.G. Evans, J.W. Hutchinson, N.A. Fleck, M.F. Ashby, H.N.G. Wadley, The topological
651 design of multifunctional cellular metals, Progress in Materials Science. 46(3) (2001) 309-
652 327, https://doi.org/10.1016/S0079-6425(00)00016-5.
653 [23] Y. Lin, W. Shi, J. Li, Y. Liu, S. Liu, J. Li, Evaluation of mechanical properties of Ti–
654 6Al–4V BCC lattice structure with different density gradient variations prepared by L-PBF,
655 Materials Science and Engineering: A. 872 (2023) 144986,
656 https://doi.org/10.1016/j.msea.2023.144986.
657 [24] L. Zhang, S. Feih, S. Daynes, S. Chang, M.Y. Wang, J. Wei, W.F. Lu, Energy absorption
658 characteristics of metallic triply periodic minimal surface sheet structures under compressive
659 loading, Additive Manufacturing. 23 (2018) 505-515,
660 https://doi.org/10.1016/j.addma.2018.08.007.
661 [25] S.J. Li, Q.S. Xu, Z. Wang, W.T. Hou, Y.L. Hao, R. Yang, L.E. Murr, Influence of cell
662 shape on mechanical properties of Ti-6Al-4V meshes fabricated by electron beam melting
663 method, Acta Biomater. 10(10) (2014) 4537-47, 10.1016/j.actbio.2014.06.010.
664 [26] S. Rajagopalan, R.A. Robb, Schwarz meets Schwann: Design and fabrication of
665 biomorphic and durataxic tissue engineering scaffolds, Medical Image Analysis. 10(5) (2006)
666 693-712, https://doi.org/10.1016/j.media.2006.06.001.
667 [27] D. Ouyang, N. Li, L. Liu, Structural heterogeneity in 3D printed Zr-based bulk metallic
668 glass by selective laser melting, J Alloy Compd. 740 (2018) 603-609,
669 https://doi.org/10.1016/j.jallcom.2018.01.037.

[28] G. Yang, X. Lin, F. Liu, Q. Hu, L. Ma, J. Li, W. Huang, Laser solid forming Zr-based bulk metallic glass, Intermetallics. 22 (2012) 110-115, https://doi.org/10.1016/j.intermet.2011.10.008.
[29] L.-Y. Chen, S.-X. Liang, Y. Liu, L.-C. Zhang, Additive manufacturing of metallic lattice structures: Unconstrained design, accurate fabrication, fascinated performances, and challenges, Materials Science and Engineering: R: Reports. 146 (2021) 100648, https://doi.org/10.1016/j.mser.2021.100648.
[30] L.J. Gibson, M.F. Ashby, Cellular solids : structure & properties, 2nd ed., Cambridge University Press, Cambridge, 1997.
[31] L.J. Gibson, M.F. Ashby, B.A. Harley, M.F. Ashby, B.A. Harley, Cellular materials in nature and medicine, Cambridge University Press, Cambridge ; New York, 2010.
[32] L. Zhang, B. Song, L. Yang, Y. Shi, Tailored mechanical response and mass transport characteristic of selective laser melted porous metallic biomaterials for bone scaffolds, Acta Biomater. 112 (2020) 298-315, https://doi.org/10.1016/j.actbio.2020.05.038.
[33] O. Alketan, R. Abu Al-Rub, R. Rowshan, The effect of architecture on the mechanical properties of cellular structures based on the IWP minimal surface, Journal of Materials Research. 33 (2018) 1-17, https://doi.org/10.1557/jmr.2018.1.
[34] O. Alketan, R. Rowshan, R. Abu Al-Rub, Topology-Mechanical Property Relationship of 3D Printed Strut, Skeletal, and Sheet Based Periodic Metallic Cellular Materials, Additive Manufacturing. 19 (2018) 167–183, https://doi.org/10.1016/j.addma.2017.12.006.
[35] J. Song, Y. Wang, W. Zhou, R. Fan, B. Yu, Y. Lu, L. Li, Topology optimization-guided lattice composites and their mechanical characterizations, Composites Part B: Engineering. 160 (2019) 402-411, https://doi.org/10.1016/j.compositesb.2018.12.027.
[36] M. Mieszala, M. Hasegawa, G. Guillonneau, J. Bauer, R. Raghavan, C. Frantz, O. Kraft, S. Mischler, J. Michler, L. Philippe, Micromechanics of Amorphous Metal/Polymer Hybrid Structures with 3D Cellular Architectures: Size Effects, Buckling Behavior, and Energy Absorption Capability, Small. 13(8) (2017) 1602514, https://doi.org/10.1002/smll.201602514.
[37] L.J. Gibson, M.F. Ashby, The Mechanics of Three-Dimensional Cellular Materials, Proceedings of the Royal Society of London. Series A, Mathematical and Physical Sciences. 382(1782) (1982) 43-59, https://doi.org/10.1098/rspa.1982.0088.
[38] L.J. Gibson, M.F. Ashby, G.S. Schajer, C.I. Robertson, The Mechanics of Two-Dimensional Cellular Materials, P Roy Soc Lond a Mat. 382(1782) (1982) 25-42, https://doi.org/10.1098/rspa.1982.0087.
[39] S. Wu, L. Yang, X. Yang, P. Chen, J. Su, H. Wu, Z. Liu, H. Wang, C. Wang, C. Yan, Y. Shi, Mechanical properties and energy absorption of AlSi10Mg Gyroid lattice structures fabricated by selective laser melting, Smart Manufacturing. 01(01) (2022) 2150001, https://doi.org/10.1142/S2737549821500010.
[40] M. Mazur, M. Leary, S. Sun, M. Vcelka, D. Shidid, M. Brandt, Deformation and failure behaviour of Ti-6Al-4V lattice structures manufactured by selective laser melting (SLM), The International Journal of Advanced Manufacturing Technology. 84(5) (2016) 1391-1411, https://doi.org/10.1007/s00170-015-7655-4.

712 [41] H. Yin, Z. Liu, J. Dai, G. Wen, C. Zhang, Crushing behavior and optimization of sheet-
713 based 3D periodic cellular structures, Composites Part B: Engineering. 182 (2020) 107565,
714 https://doi.org/10.1016/j.compositesb.2019.107565.
715 [42] L. Zhang, S. Feih, S. Daynes, S. Chang, M.Y. Wang, J. Wei, W.F. Lu, Pseudo-ductile
716 fracture of 3D printed alumina triply periodic minimal surface structures, Journal of the
717 European Ceramic Society. 40(2) (2020) 408-416,
718 https://doi.org/10.1016/j.jeurceramsoc.2019.09.048.
719
720

Supplemental Materials

Congrui Yang[1, 2], Di Ouyang[1,3], Lei Zhang[3], Yongyun Zhang[1, 2], Xing Tong[2], Haibo Ke[2*], K.C. Chan[1*], Weihua Wang[2,4]

1. Research Institute for Advanced Manufacturing, Department of Industrial and Systems Engineering, The Hong Kong Polytechnic University, Hong Kong, China.

2. Songshan Lake Materials Laboratory, Dongguan, 523808, China

3. State Key Laboratory of Material Processing and Die & Mould Technology and School of Materials Science and Engineering, Huazhong University of Science and Technology, Wuhan, 430074, China

4. Institute of Physics, Chinese Academy of Sciences, Beijing 100190, China

* Corresponding author.
E-mail address: kc.chan@polyu.hk (Kang Cheung Chan), kehaibo@sslab.org.cn (Haibo Ke)

1. **Solid parent material property**

The representative uniaxial compression stress versus strain response was presented in Fig. S1. The solid parent 3D-printed Zr based BMG under 19.23 J/mm3 energy density has a compressive strength of 1509 MPa and Young's modulus of 72.0GPa. This data use for normalizing the compressive strength and elastic modulus for MG lattices in this study. 3D printed Zr based BMG only have the elastic stage, thus, linear explicit finite element method was applied to study the stress distribution of BCC lattices. And the discussion based on the simulation results only focus on the elastic stage, to ensure the reliability of simulation results.

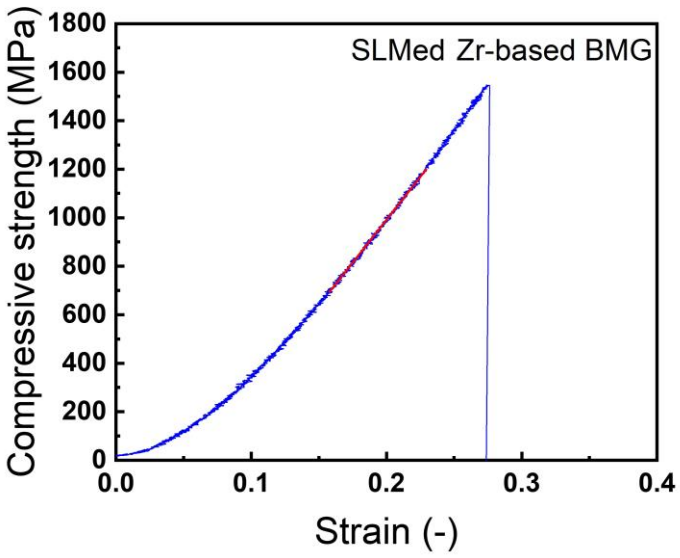

Fig S1. Representative uniaxial compressive stress versus strain response of L-PBF-built Zr-based BMG.

762 2. **Geometrical specifications of the BMG lattices used in this study.**

763 **Table S1. Geometrical specifications of the BCC and TPMS lattices used in this study.**

Lattice sample code	Nominal shell thickness (mm)	Strut Diameter (mm)	Strut length of Unit Cell (mm)	Unit cell size (mm)	Number of cells (x,y,z)
D0.8L4.0	/	0.8	4.0	2.31× 2.31×2.31	(4,4,4)
D0.8L3.6	/	0.8	3.6	2.10 × 2.10 × 2.10	(4,4,4)
D0.8L3.2	/	0.8	3.2	1.85 × 1.85 × 1.85	(4,4,4)
D0.8L2.8	/	0.8	2.8	1.62 × 1.62 × 1.62	(4,4,4)
T293	293	/	/	2.5 × 2.5× 2.5	(4,4,4)
T345	345	/	/	2.5 × 2.5× 2.5	(4,4,4)
T403	403	/	/	2.5 × 2.5× 2.5	(4,4,4)
T468	468	/	/	2.5 × 2.5× 2.5	(4,4,4)

764

765